Supplementary materials

Bismuth Nanosheets Derived by in-situ Morphology Transformation of Bismuth Oxides for Selective Electrochemical CO_2 Reduction to Formate

Jungkuk Lee, Hengzhou Liu, Yifu Chen, Wenzhen Li*

Department of Chemical and Biological Engineering, Iowa State University, Ames, Iowa 50011, United States

*Corresponding Author: wzli@iastate.edu

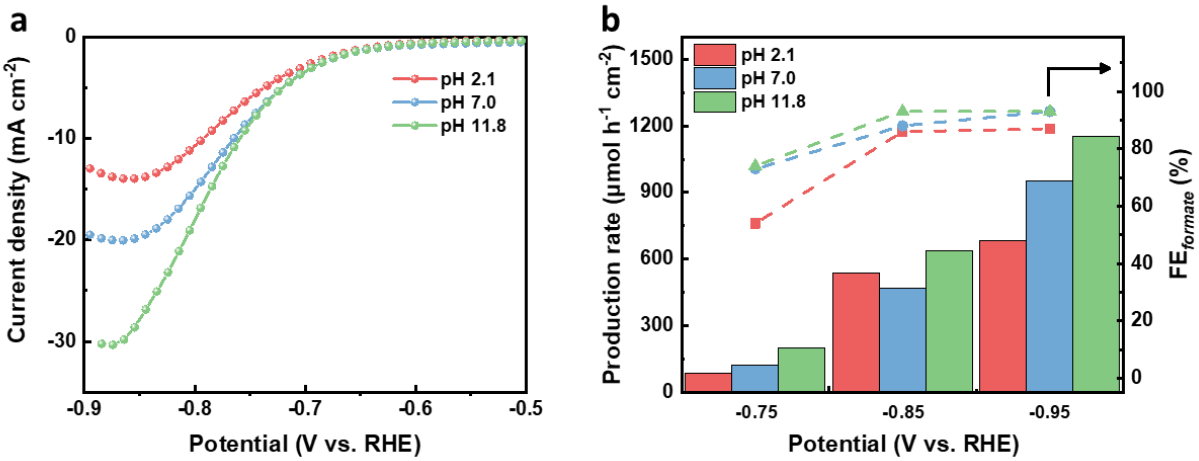

Figure S1. Effect of pH on Bi_2O_3 synthesis for CO_2RR performance. (a) LSV curves in CO_2-saturated 0.5 M $KHCO_3$ at scan rate of 10 mV s^{-1}. (b) Production rate and FE.

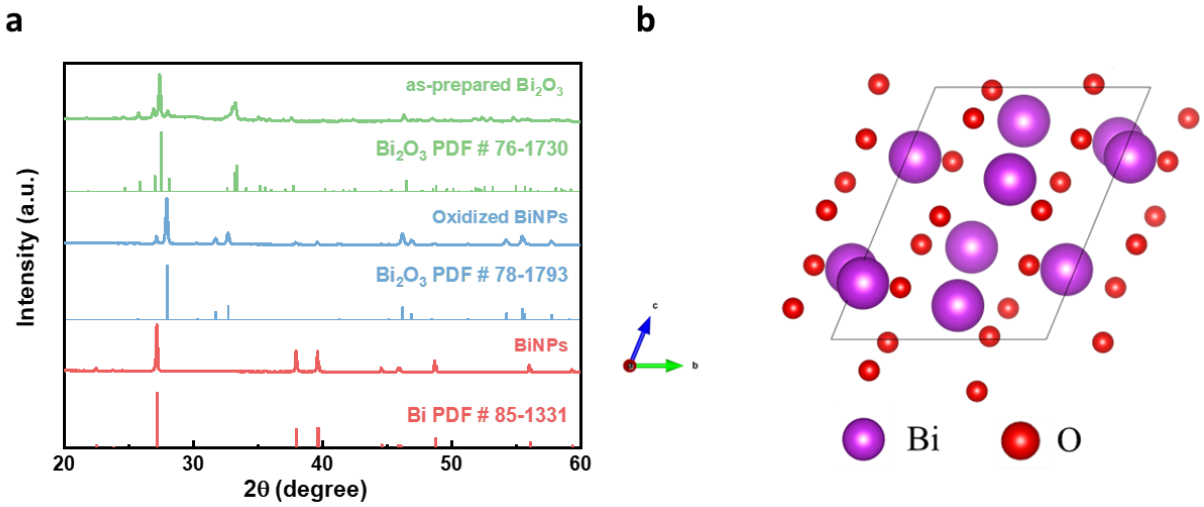

Figures S2. (a) XRD patterns of BiNPs, Oxi-BiNPs, and as-prepared Bi_2O_3. (b) Crystal structure of Bi_2O_3.

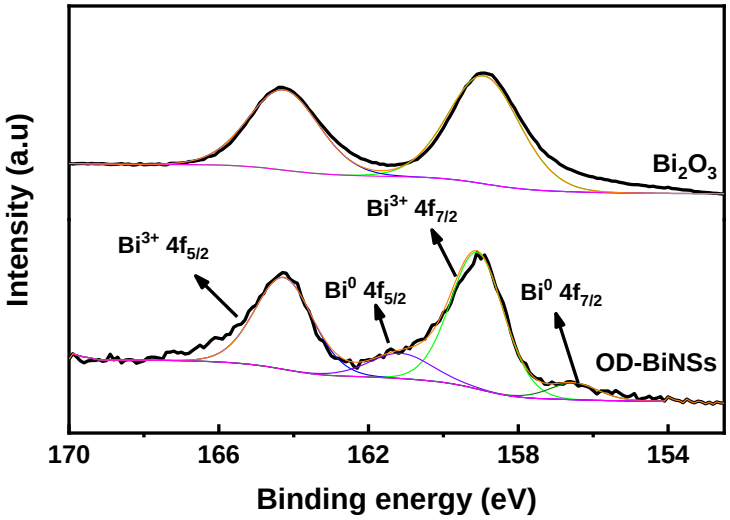

Figures S3. XPS of Bi_2O_3 (before CV) and OD-BiNSs (after CV).

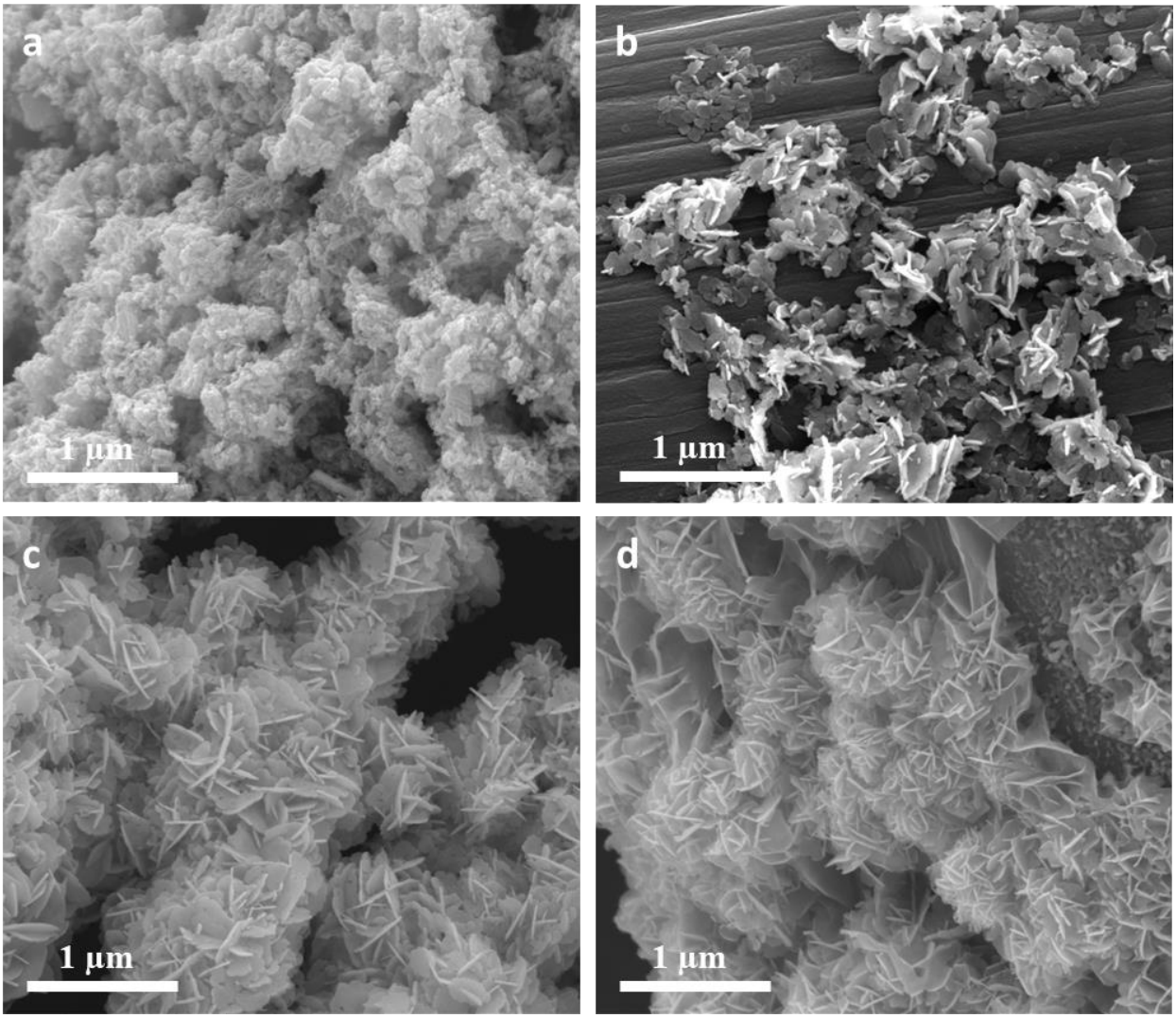

Figure S4. SEM images of Bi_2O_3 with different numbers of CV cycles. (a) Before CV, (b) 1 cycle, (c) 2 cycles, and (d) 20 cycles.

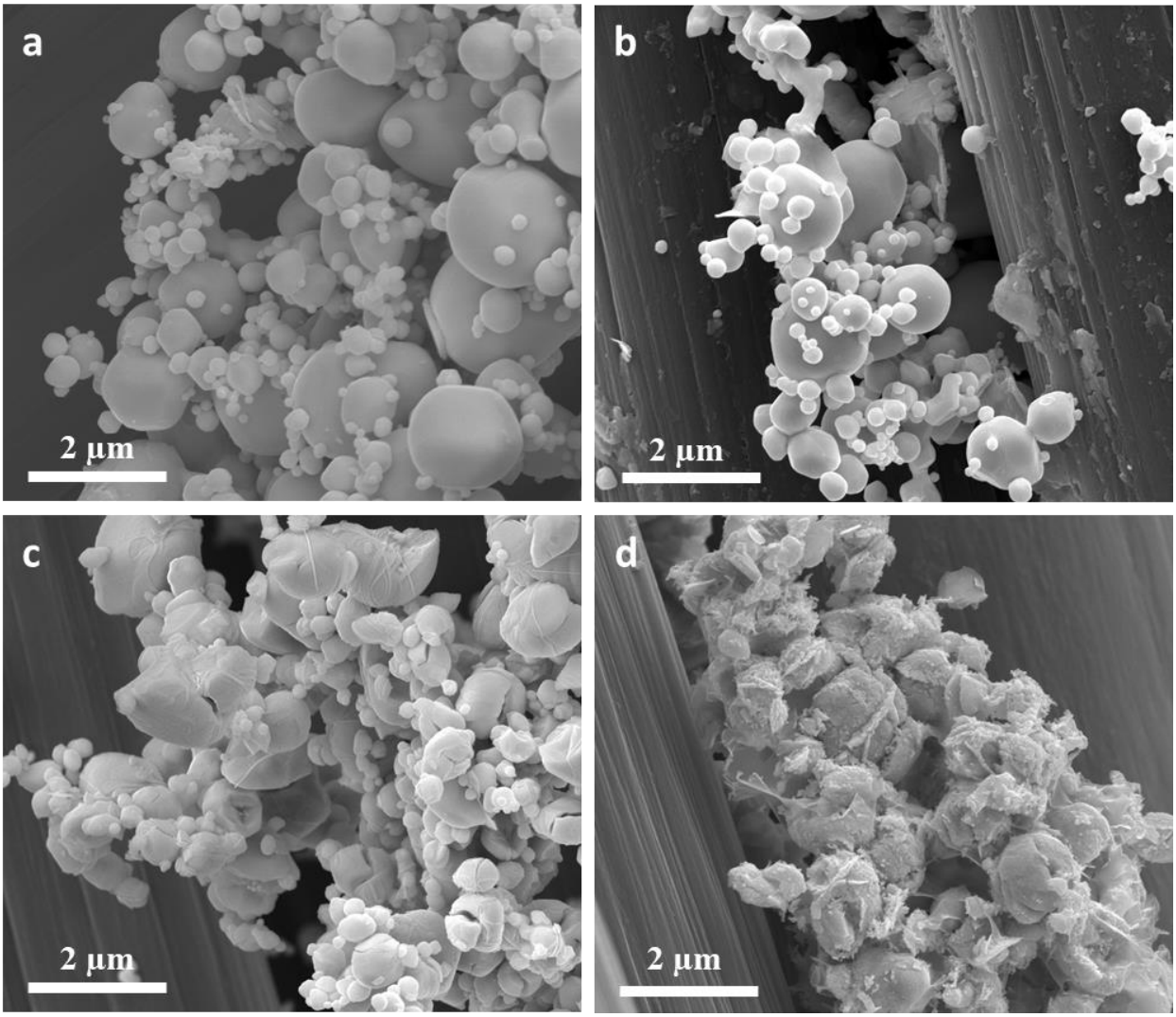

Figure S5. SEM images of (a,b) BiNPs and (c,d) Oxi-BiNPs before and after 20 cycles of CV, respectively.

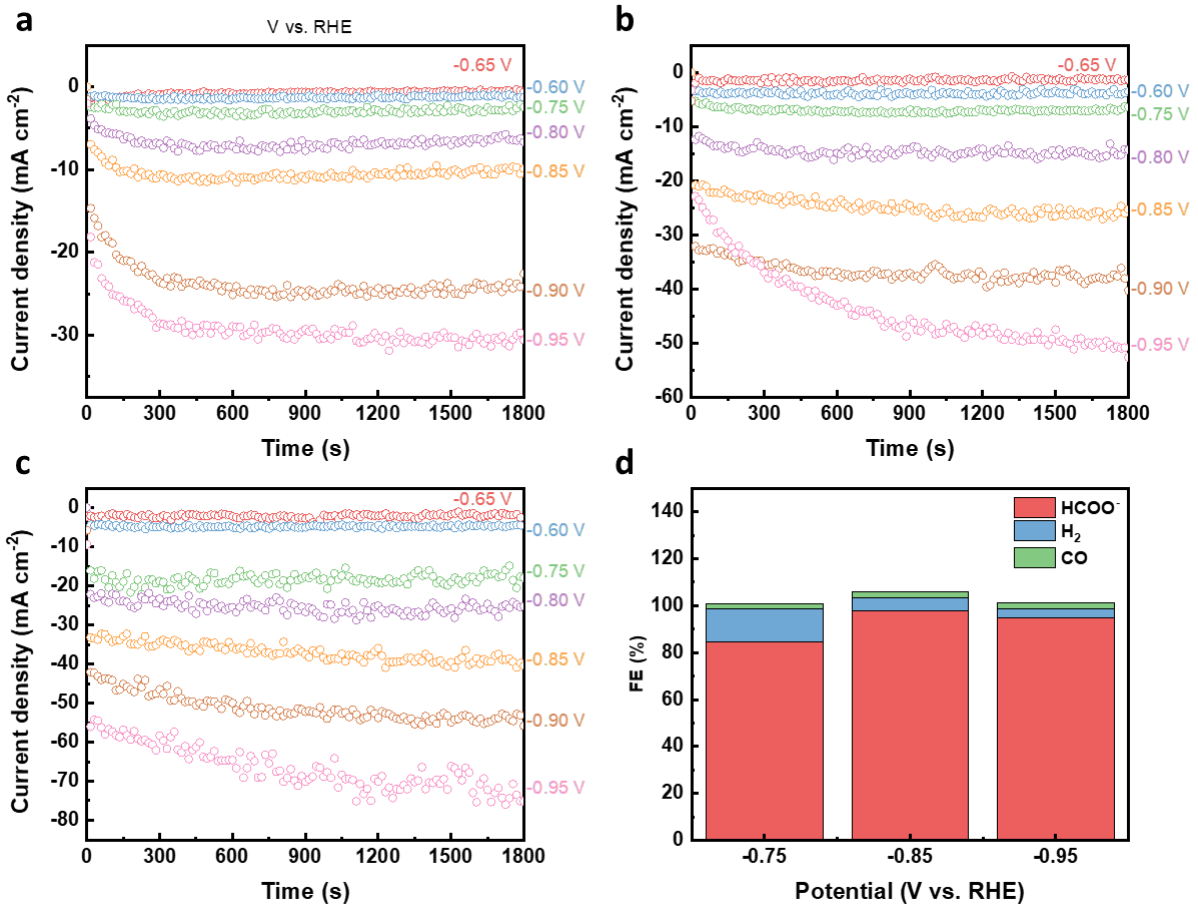

Figure S6. Current density profiles of (a) BiNPs, (b) Oxi-BiNPs, and (c) OD-BiNPs under different applied potentials, and (d) Faradaic efficiencies for different products of OD-BiNSs.

Gaseous products were analyzed by on-line gas chromatography (GC, SRI instrument 8610C MG#3) equipped with HaySep D and MolSieve 5 Å columns. H_2 and CO were detected by the thermal conductivity detector (TCD) and flame ionization detector (FID), respectively. The rate of H_2 and CO generation (r, mol s^{-1}) was calculated by:

$$r = c \times 10^{-6} \times [p\dot{V} \times 10^{-6}/(RT)]$$

Where c is the H_2 or CO concentration (ppm); $\dot{V}$ is the volumetric flow rate of the inlet gas (20 mL min^{-1}); p is the ambient pressure ($p = 1.013 \times 10^5$ Pa); R is the gas constant (R = 8.314 J mol^{-1}

K^{-1}); T is the room temperature (293.15 K). The total amount of H_2 and CO production (mol) was calculated by integrating the plot of H_2 and CO production rate (mol s^{-1}) vs. reaction time (s) with polynomial curve fitting.

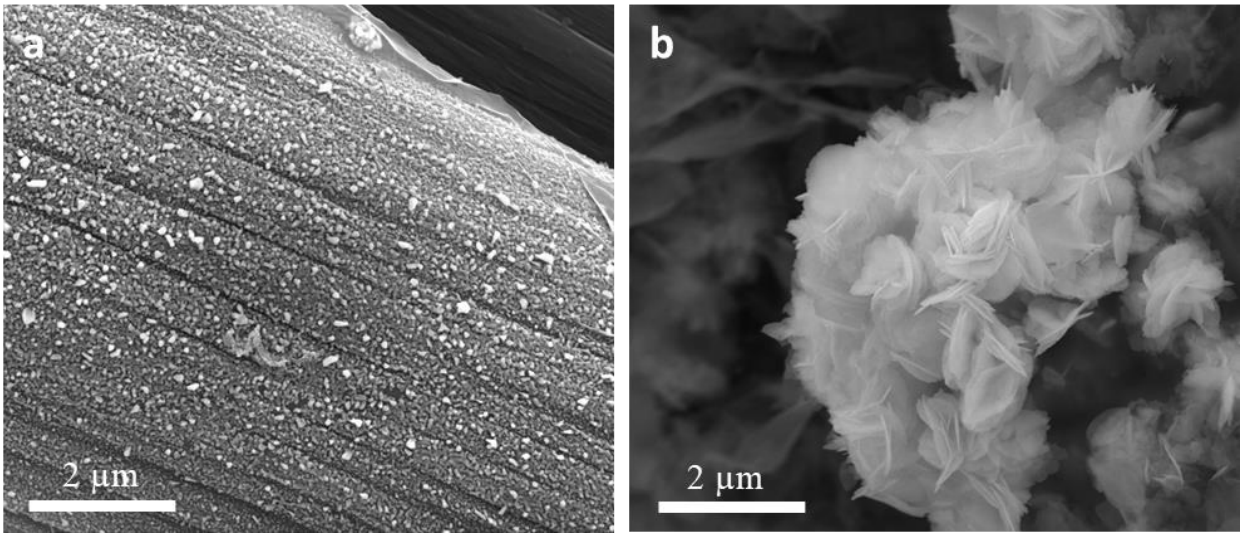

Figure S7. SEM images of (a) BiNPs after 30 min of CO_2RR at $-0.85V_{RHE}$ and (b) OD-BiNSs after 10 h stability test at $-0.85V_{RHE}$.

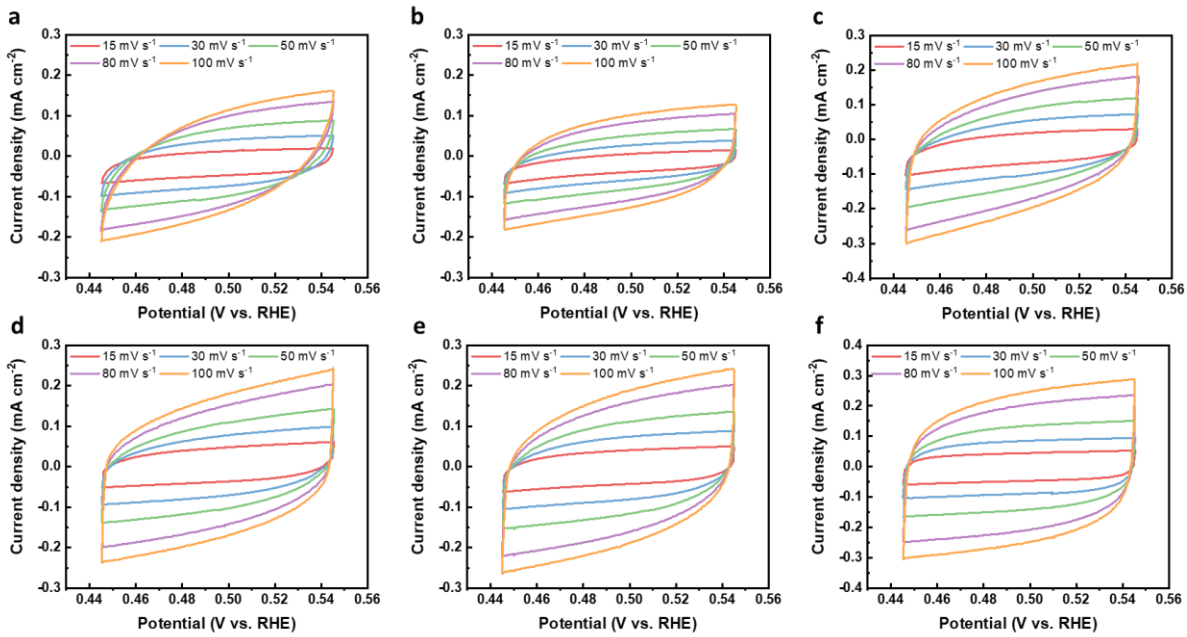

Figure S8. CV curve for the measurement of C_{dl} for (a,d) BiNPs, (b,e) Oxi-BiNPs, and (c,f) OD-BiNSs before and after 20 cycles of CV, respectively.

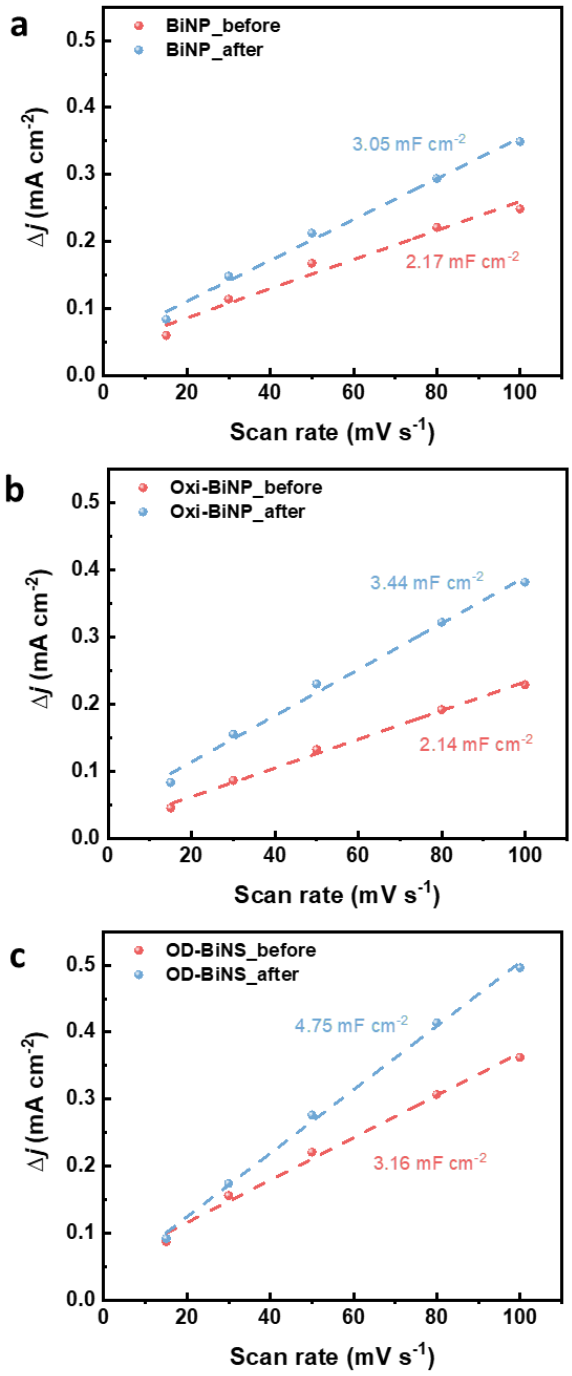

Figure S9. Comparison of C_{dl} before and after CV over (a) BiNPs, (b) Oxi-BiNPs, and (c) OD-BiNSs.

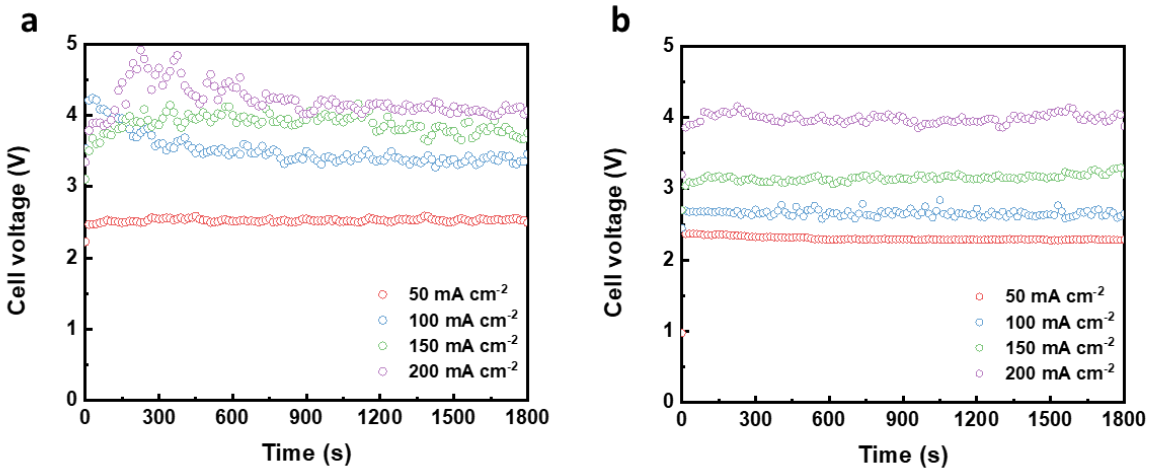

Figure S10. Cell voltage profiles during the chronopotentiometry experiments in the flow cell over (a) BiNPs and (b) OD-BiNSs.

Table S1. Comparison of CO_2RR performance of state-of-the-art Bi-based catalysts in H-type cells.

Catalysts	FE (%)	Current density (mA cm^{-2})	Potential (V_{RHE})	Electrolyte concentration	Reference
OD-BiNSs	93	62	−0.95	0.5 M $KHCO_3$	This work
	92	47	−0.9		
Bi nanotube	97.1	32.1	−0.9	0.5 M $KHCO_3$	1
Bi nanowire	95	15	−0.69	0.5 M $NaHCO_3$	2
Electrodeposited BiNS	93	30	−0.89	0.5 M $NaHCO_3$	3
3D-porous Bi-ene	95	50	−0.87	0.5 M $KHCO_3$	4
BiOBr derived BiNS	95	55	−0.9	0.1 M $KHCO_3$	5
Bi_2O_3 nanotube	93	10	−0.7	0.5 M $KHCO_3$	6
Bi nanostructure	92	18	−0.9	0.5 M $KHCO_3$	7
Bi_2O_3@MOF derived carbon nanorode	93.8	15	−1.256	0.5 M $KHCO_3$	8

Table S2. Comparison of CO_2RR performance on state-of-the-art Bi-based catalysts in flow cells.

Catalysts	Membrane*	FE (%)	Current density (mA cm^{-2})	Potential	Electrolyte (catholyte /anolyte)	Reference
OD-BiNSs	CEM	95	200	4.0 V (full-cell)	0.5 M $KHCO_3$ /1.0 M KOH	This work
		99	100	2.6 V (full-cell)		
Alloyed BiSn	AEM	87.8	90	3.36 V (full-cell)	n/a /0.5 M $KHCO_3$	9
		92.8	180	4.06 V (full-cell)		
	CEM	68.5	90	3.98 V (full-cell)		
		43	120	4.27 V (full-cell)		
Hydrangea-like BiNS	BPM	95	17	3.0 V (full-cell)	0.5 M $KHCO_3$ /1.0 M KOH	21
Electrodeposited Bi	BPM	64	100	4.0 V (full-cell)	3.0 M $KHCO_3$ /1.0 M KOH	10
$BiVO_4$ derived Bismuthene	AEM	-	50	4.25 V (full-cell)	1.0 M $KHCO_3$ /1.0 M $KHCO_3$	11

Metal-organic layer derived Bismuthene	BPM	98.5	18	3.0 V (full-cell)	0.5 M $KHCO_3$ /1.0 M KOH	12
Bi_2O_3@MOF derived carbon nanorode	AEM	93	208	−1.1 V_{RHE} (half-cell)	1.0 M KOH /1.0 M KOH	8
3D-porous Bi-ene	AEM	95	200	−0.7 V_{RHE} (half-cell)	1M KOH /not specified	4

* Membrane: Cation exchange membrane (CEM), Anion exchange membrane (AEM), Bipolar membrane (BPM)

Table S3. Summary of the synthesis conditions of Bi-based catalysts for CO_2RR.

Catalyst	Precursor and solvent	Synthesis conditions	Reference
OD-BiNSs	$Bi(NO_3)_3·5H_2O$ in KOH solution	room-temperature	This work
BMNS	$Bi(NO_3)_3·5H_2O$ + H_2BDC in DMF	70°C	13
Bi5O7I NSs	Bi flakes in NaI solution	direct current (DC) potential of 20 V	14
BiNSs	$Bi(Cl)_3$ in 2-ethoxyethanol	120°C	15
Ultrathin BiNS	$Bi(NO_3)_3$ + KI in glacial acetic acid	160°C	16
BiOBr derived BiNS	$BiBr_3$ in DMSO	140°C	5
distorted BiOCl nanoplates	$Bi(NO_3)_3·5H_2O$ in mannitol	160°C autoclave (20 Mpa)	17
Metal-organic layer derived Bismuthene	$Bi(NO_3)_3·5H_2O$ + H_2IDC in piperazine solutions	170°C autoclave	12
$BiPO_4$	$Bi(NO_3)_3·5H_2O$ + $Na_3PO4·12H_2O$ in ethylene glycol	170°C autoclave	18
Bi_2O_3@MOF derived carbon nanorode	$Bi(NO_3)_2·5H_2O$ + H_3BTC in methanol anhydrous	120°C autoclave + 800°C heating	8
nBuLi-Bi	nBuLi in hexanes	80°C	19
Bi_2O_3 nanotube	bismuth acetate + PVP in ethylene glycol	300°C	6
f-Bi_2O_3	bismuth(III) 2-ethylhaxnoate + 2-ethylhexanoic acid in Toluene	4 bar	20
S-Bi-NSs	$Bi(NO_3)_3·5H_2O$ in Glycerol and DMF	160°C autoclave	21
$BiVO_4$ derived Bismuthene	$Bi(NO_3)_3·5H_2O$ + NH_4VO_3 in SDBS solutions	200°C autoclave + 300°C heating	11
2D-Bi	$Bi(NO_3)_2·5H_2O$ + CTAB + urea in ethanol	90°C	22

REFERENCES

(1) Zheng, H.; Wu, G.; Gao, G.; Wang, X. The Bismuth Architecture Assembled by Nanotubes Used as Highly Efficient Electrocatalyst for CO_2 Reduction to Formate. *Chem. Eng. J*. **2021**, 421, 129606.

(2) Zhang, X.; Sun, X.; Guo, S.-X.; Bond, A.M.; Zhang, J. Formation of Lattice-Dislocated Bismuth Nanowires on Copper Foam for Enhanced Electrocatalytic CO_2 Reduction at Low Overpotential, *Energy Environ. Sci*. **2019**, 12, 1334-1340.

(3) Guo, S.X.; Zhang, Y.; Zhang, X.; Easton, C.D.; MacFarlane, D.R.; Zhang, J. Phosphomolybdic Acid-Sssisted Growth of Ultrathin Bismuth Nanosheets for Enhanced Electrocatalytic Reduction of CO_2 to Formate, *ChemSusChem* **2019**, 12, 1091-1100.

(4) Zhang, M.; Wei, W.; Zhou, S.; Ma, D.-D.; Cao, A.; Wu, X.-T.; Zhu, Q.-L. Engineering a Conductive Network of Atomically Thin Bismuthene With Rich Defects Enables CO_2 Reduction to Formate with Industry-Compatible Current Densities and Stability. *Energy Environ. Sci*. **2021**, 14 4998-5008.

(5) Garcia de Arquer, F.P.; Bushuyev, O.S.; De Luna, P.; Dinh, C.T.; Seifitokaldani, A.; Saidaminov, M.I.; Tan, C.S.; Quan, L.N.; Proppe, A.; Kibria, M.G.; Kelley, S.O.; Sinton, D.; Sargent, E.H. 2D Metal Oxyhalide-Derived Catalysts for Efficient CO_2 Electroreduction. *Adv. Mater*, **2018**, 30, 1802858.

(6) Gong, Q.; Ding, P.; Xu, M.; Zhu, X.; Wang, M.; Deng, J.; Ma, Q.; Han, N.; Zhu, Y.; Lu, J.; Feng, Z.; Li, Y.; Zhou, W.; Li, Y. Structural Defects on Converted Bismuth Oxide Nanotubes Enable Highly Active Electrocatalysis of Carbon Dioxide Reduction, *Nat*

Commun. **2019**, 10, 2807.

(7) Lu, P.; Gao, D.; He, H.; Wang, Q.; Liu, Z.; Dipazir, S.; Yuan, M.; Zu, W.; Zhang, G. Facile Synthesis of a Bismuth Nanostructure with Enhanced Selectivity for Electrochemical Conversion of CO_2 to Formate, *Nanoscale*, **2019**, 11, 7805-7812.

(8) Deng, P.; Yang, F.; Wang, Z.; Chen, S.; Zhou, Y.; Zaman, S.; Xia, B.Y. Metal-Organic Framework-Derived Carbon Nanorods Encapsulating Bismuth Oxides for Rapid and Selective CO_2 Electroreduction to Formate, *Angew. Chem. Int. Ed*. **2020**, 59, 10807-10813.

(9) Li, L.; Ozden, A.; Guo, S.; García de Arquer, F.P.; Wang, C.; Zhang, M.; Zhang, J.; Jiang, H.; Wang, W.; Dong, H.; Sinton, D.; Sargent, E.H.; Zhong, M. Stable, Active CO_2 Reduction to Formate via Redox-Modulated Stabilization of Active Sites, *Nat. Commun.* **2021**, 12, 5223.

(10) Li, T.; Lees, E.W.; Zhang, Z.; Berlinguette C.P. Conversion of Bicarbonate to Formate in an Electrochemical Flow Reactor, *ACS Energy Lett*. **2020**, 5, 2624-2630.

(11) Ma, W.; Bu, J.; Liu, Z.; Yan, C.; Yao, Y.; Chang, N.; Zhang, H.; Wang, T.; Zhang, J. Monoclinic Scheelite Bismuth Vanadate Derived Bismuthene Nanosheets with Rapid Kinetics for Electrochemically Reducing Carbon Dioxide to Formate. *Adv. Funct. Mater*. **2020**, 31, 2006704.

(12) Cao, C.; Ma, D.D.; Gu, J.F.; Xie, X.; Zeng, G.; Li, X.; Han, S.G.; Zhu, Q.L.; Wu, X.T.; Xu, Q. Metal-Organic Layers Leading to Atomically Thin Bismuthene for Efficient Carbon Dioxide Electroreduction to Liquid Fuel. *Angew. Chem. Int. Ed*. **2020**, 59, 15014-15020.

(13) Li, N.; Yan, P.; Tang, Y.; Wang, J.; Yu, X.-Y.; Wu, H. B. In-situ Formation of Ligand-Stabilized Bismuth Nanosheets for Efficient CO_2 Conversion. *Appl. Catal. B.* **2021**, 297, 120481.

(14) Wang, D.; Chang, K.; Zhang, Y.; Wang, Y.; Liu, Q.; Wang, Z.; Ding, D.; Cui, Y.; Pan, C.; Lou, Y. Unravelling the Electrocatalytic Activity of Bismuth Nanosheets Towards Carbon Dioxide Reduction: Edge plane versus Basal plane. *Appl. Catal. B.* **2021**, 299, 120693.

(15) Yang, F.; Elnabawy, A. O.; Schimmenti, R.; Song, P.; Wang, J.; Peng, Z.; Yao, S.; Deng, R.; Song, S.; Lin, Y. Bismuthene for Highly Efficient Carbon Dioxide Electroreduction Reaction. *Nat. commun*. **2020**, 11, 1-8.

(16) Han, N.; Wang, Y.; Yang, H.; Deng, J.; Wu, J.; Li, Y.; Li, Y. Ultrathin Bismuth Nanosheets from In situ Topotactic Transformation for Selective Electrocatalytic CO_2 Reduction to Formate. *Nat. commun*. **2018**, 9, 1-8.

(17) Zhou, Y.; Yan, P.; Jia, J.; Zhang, S.; Zheng, X.; Zhang, L.; Zhang, B.; Chen, J.; Hao, W.; Chen, G. Supercritical CO_2-Constructed Intralayer $[Bi_2O_2]^{2+}$ Structural Distortion for Enhanced CO_2 Electroreduction. *J. Mater. Chem. A* **2020**, 8, 13320-13327.

(18) Wang, Y.; Li, Y.; Liu, J.; Dong, C.; Xiao, C.; Cheng, L.; Jiang, H.; Jiang, H.; Li, C. $BiPO_4$-Derived 2D Nanosheets for Efficient Electrocatalytic Reduction of CO_2 to Liquid Fuel. *Angew. Chem.Int. Ed.* **2021**, 60, 7681-7685.

(19) Fan, L.; Xia, C.; Zhu, P.; Lu, Y.; Wang, H. Electrochemical CO_2 Reduction to High-Concentration Pure Formic Acid Solutions in an All-Solid-State Reactor. *Nat. commun.*

2020, 11, 1-9.

(20) Tran-Phu, T.; Daiyan, R.; Fusco, Z.; Ma, Z.; Amal, R.; Tricoli, A. Nanostructured β-Bi_2O_3 Fractals on Carbon Fibers for Highly Selective CO_2 Electroreduction to Formate. *Adv. Funct. Mater*. **2020**, 30, 1906478.

(21) Peng, C.-J.; Zeng, G.; Ma, D.-D.; Cao, C.; Zhou, S.; Wu, X.-T.; Zhu, Q.-L. Hydrangea-like Superstructured Micro/Nanoreactor of Topotactically Converted Ultrathin Bismuth Nanosheets for Highly Active CO_2 Electroreduction to Formate. *ACS Appl. Mater. Interfaces*. **2021**, 13, 20589-20597.

(22) Xia, C.; Zhu, P.; Jiang, Q.; Pan, Y.; Liang, W.; Stavitski, E.; Alshareef, H. N.; Wang, H. Continuous Production of Pure Liquid Fuel Solutions via Electrocatalytic CO_2 Reduction Using Solid-Electrolyte Devices. *Nat. Energy* **2019**, 4, 776-785.